Ultramicroscopy 171 (2016) 126–138

Contents lists available at ScienceDirect

Ultramicroscopy

journal homepage: www.elsevier.com/locate/ultramic

Angle selective backscattered electron contrast in the low-voltage scanning electron microscope: Simulation and experiment for polymers

Q. Wan [a,*], R.C. Masters [a], D. Lidzey [b], K.J. Abrams [a], M. Dapor [c], R.A. Plenderleith [a], S. Rimmer [d], F. Claeyssens [a], C. Rodenburg [a]

[a] Department of Material Science and Engineering, University of Sheffield, Western Bank, Sheffield S10 2TN, UK
[b] Department of Physics and Astronomy, University of Sheffield, Western Bank, Sheffield S10 2TN, UK
[c] European Centre for Theoretical Studies in Nuclear Physics and Related Areas (ECT*-FBK) and Trento Institute for Fundamental Physics and Applications (TIFPA-INFN), via Sommarive 18, I-38123 Trento, Italy
[d] Department of Chemistry, University of Sheffield, Western Bank, Sheffield S10 2TN, UK

ARTICLE INFO

Article history:
Received 17 May 2016
Received in revised form
2 September 2016
Accepted 11 September 2016
Available online 15 September 2016

Keywords:
Low-voltage scanning electron microscopy
Quantitative back-scattered imaging
Polymer
Concentric back scattered detector
Angle selective SEM

ABSTRACT

Recently developed detectors can deliver high resolution and high contrast images of nanostructured carbon based materials in low voltage scanning electron microscopes (LVSEM) with beam deceleration. Monte Carlo Simulations are also used to predict under which exact imaging conditions purely compositional contrast can be obtained and optimised. This allows the prediction of the electron signal intensity in angle selective conditions for back-scattered electron (BSE) imaging in LVSEM and compares it to experimental signals. Angle selective detection with a concentric back scattered (CBS) detector is considered in the model in the absence and presence of a deceleration field, respectively. The validity of the model prediction for both cases was tested experimentally for amorphous C and Cu and applied to complex nanostructured carbon based materials, namely a Poly(N-isopropylacrylamide)/Poly(ethylene glycol) Diacrylate (PNIPAM/PEGDA) semi-interpenetration network (IPN) and a Poly(3-hexylthiophene-2,5-diyl) (P3HT) film, to map nano-scale composition and crystallinity distribution by avoiding experimental imaging conditions that lead to a mixed topographical and compositional contrast

© 2016 The Authors. Published by Elsevier B.V. This is an open access article under the CC BY license (http://creativecommons.org/licenses/by/4.0/).

1. Introduction

Low-voltage scanning electron microscopes (LVSEMs) have substantially benefited from the development of the field-emission gun and high sensitivity detectors in last few decades [1]; resulting in a significant increase of resolution from 100 nm to <0.5 nm [2]. Nowadays, the LVSEM is commonly used as a high resolution imaging for surface topography and insulators [3].

In the case of imaging insulator materials, it is well known the SE signal is highly sensitive to charging on the sample surface, voltage contrast will also form as a result of the charging effect [4]. Although BSE imaging is generally less affected by surface charging, the electric field build up on sample surface can still cause electron beam deflection and strong electron implantation effect which leads to sample damage [5,6], especially if the primary beam energy exceeds a few keV as in conventional BSE imaging. In order to prevent the charging situation, ordinarily, a conductive coating is applied in conventional SEM. Unfortunately this coating hides the surface detail and can create artificial signals due to the electron range differences in the sample material and the coating [7]. In contrast, the LVSEM technique allows careful control of the primary voltage which allows for the imaging of non-conductive insulating materials, even in the absence of a coating [8].

Additionally, for a composition based investigation, low-voltage backscattered (LVBSE) imaging can provide relatively high imaging resolutions up to <5 nm [9]. Since the electron range is significantly decreased in LVBSE imaging [6], a non- coated specimen is strongly preferred for a quantitative analysis. In the absence of a conductive coating, the primary electron energy is limited to a small energy range in which the electron input and emission is close to balance. The BSE signal can be optimised for uncoated insulating samples and, generally, reaches a maximum value around primary energy setting of 1–2 keV [4,10].

To optimise the LVBSE imaging, Monte Carlo (MC) simulations are required to predict the image contrast, as conventional calculation methods yield large deviations when the primary electron energy drops below 2 keV [11]. Such MC simulations normally comprise of both inelastic scattering and the elastic scattering. The

* Corresponding author.
E-mail address: qwan2@sheffield.ac.uk (Q. Wan).

http://dx.doi.org/10.1016/j.ultramic.2016.09.006
0304-3991/© 2016 The Authors. Published by Elsevier B.V. This is an open access article under the CC BY license (http://creativecommons.org/licenses/by/4.0/).

inelastic part employs the dielectric function approach as physical model in the simulation programmes and the relevant prediction for low-voltage setting has already been reported to match the experiments [12] in SE imaging. In the case of elastic scattering simulation, the Mott cross-section solved from Dirac equation was widely applied for electron energy over 100 eV [13]. It's application for simulating electron matter interactions have been reported by researchers [14–16]. Here we report on its use for the prediction of optimised angle selective BSE imaging conditions for low density materials.

Although BSE are commonly expected to exhibit compositional information, the BSE signal can also contain topographical information [17]. This is because the signal emitted from the sample contains $BSE_{I,}$ which is generated from near-surface area and applied in topographical imaging [18], and BSE_{II} which reflects purely composition information as they originate from deeper in the specimen and have undergone multiple scattering events [19]. In order to acquire compositional or topographical information separately through BSE imaging an angular selection is needed since the BSE_I are generally emitted at large angles [20]. The detailed mechanism of BSE detection and contrast formation based on scattering angle has already been discussed in literature [21]. Here we introduce MC simulation to predict the necessary experimental conditions under which a separation in the landing angle of BSE_I and BSE_{II} can be achieved.

The concentric back scattered detector or circular back scattered detector (CBS) is a multi-segment solid state high-efficiency BSE detector [22] which is composed of multiple rings which can form images simultaneously. Thus it can collect the emitted electron signal from a set angular range [23,24]. Here we show how to optimise the microscope settings in terms of angular acceptance range by combining the low detection threshold of CBS detector with a deceleration (retarding) field [25], so it becomes possible to acquire high contrast BSE images of materials with very small average atomic number differences (free from topography). Although this work is focused on carbon based polymer materials, we expect to apply this method for heavier elements analysis such as for carbides in steel [26]. As the experimental settings for LVBSE imaging can vary greatly when a deceleration field is employed, model calculations ensure suitable imaging conditions are used to access compositional information only.

2. Theoretical background and calculations

Monte Carlo simulations can be used to calculate the electron emission from a given point at the specimen surface. This then needs to be translated into a local signal strength, $S_{D,}$ at a given point on the detector plane, based on the spatial and energy distribution of the emitted electrons as well as user-controllable parameters in the LVSEM such as the working distance and the deceleration voltage, U_d.

The angle between the incident primary beam and the straight line from emission point to detection point, $\theta_{D,}$ is shown in Fig. 2.1.1. It is defined by the working distance for $U_d=0$.

2.1. Determination of detected electron signal from the simulated electron emission

Since our calculation is focused on the signal formation in our CBS detector, only the electron signal that can potentially reach our detector is considered in the following calculation. For simplicity, we only consider the case in which the entire interaction volume is contained within the material, thus we exclude the possibility of electrons being transmitted. For any other cases the adsorbed and transmitted electrons have to be considered in more detail as the transmitted electrons could contribute to the detected signal and cause substantial contrast as was shown in literature [27]. Traditionally the electron signal detected by a SEM detector is ascribed to two parts: the secondary electron (SE) signal and the BSE signal. Thus, the overall detected electron signal strength, S_D, can be represented by Eq. (2.1.1):

$$S_D = (S_{D(BSE)} + S_{D(SE)}) \tag{2.1.1}$$

S_D is the electron signal strength measured at detection point.
$S_{D(BSE)}$ is the electron signal strength of BSE at detection point.
$S_{D(SE)}$ is the electron signal strength of SE at detection point.

Assuming $U_d = 0$, the electrons emitted with scattering angle, θ_S, move towards the detection point in a straight line from the emission point. The angle between the primary beam and the straight line from emission point to detection point written as θ_D (Fig. 2.1.1a) is equal to $\theta_{S.}$

S_D at this detection point can be estimated from following Eq. [28]:

$$S_D \propto \iint [P_{BSE}*(E_{BSE} - E_T)]dE_{BSE}d\theta_S + \iint [P_{SE}*(E_{SE} - E_T)]dE_{SE}d\theta_S \tag{2.1.2}$$

E_T is the detector energy threshold (the minimum energy that leads to a detection event which is a characteristic of the detector used).

E_{BSE} is the electron energy of a backscattered electron when it reaches the detection point.

P_{BSE} is the absolute probability of a BSE with electron energy E_{BSE} landing on this detection point.

E_{SE} is the electron energy of secondary electron when it reaches the detection point.

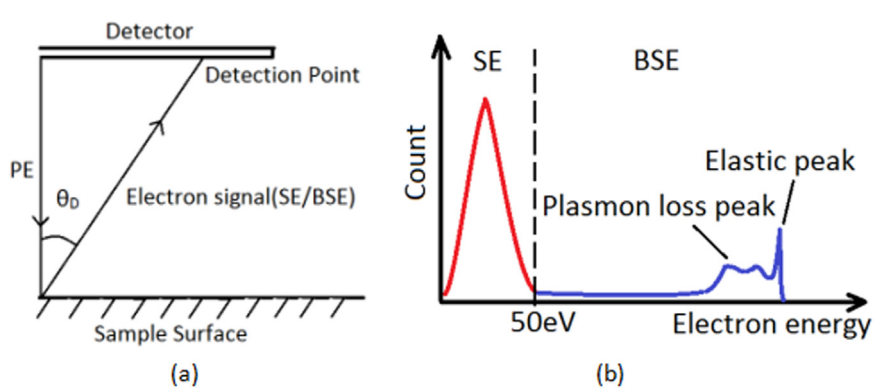

Fig. 2.1.1. (a) Schematic representation of the detection point location showing angle θ_D between the primary electron (PE) and the scattered electron and (b) Schematic of electron energy spectra illustrating the SE/BSE energy range.

P_{SE} is the absolute probability of a SE with electron energy E_{SE} landing on this detection point.

In Eq. (2.1.2), E_T is a constant for a selected detection point and a given detector. Note that our calculations are restricted to the low-loss electrons (plasmon-loss and elastic peak region, schematically shown in Fig. 2.1.1b) [29]. Thus, E_{BSE} is very close to the landing energy, U_L, of the primary electron. U_L is a parameter that is selected by the SEM user. P_{BSE} is a function of BSE scattering angle, θ_{SBSE}, and can be obtained from Monte Carlo simulations [17] using Mott cross-sections. It is based on U_L, and sample composition.

P_{SE} is a function of the SE energy, E_{SE}, and the SE scattering angle, θ_{SSE}. The latter can be obtained from Monte Carlo simulation [17] requiring electron energy loss function parameters as input. The details of the Monte Carlo simulation method we applied here are described in detail in literature [30].

In an ideal situation, a selected detection point, θ_{SBSE} and θ_{SSE} are equal to the detection angle θ_D as shown in Fig. 2.1.1a. As P_{BSE} and P_{SE} are both simulated values based on θ_D, thus,

$$\begin{cases} f(\theta) = P_{BSE}*(E_{SE} - E_T) \\ g(\theta) = P_{SE}*(E_{SE} - E_T) \end{cases}$$

We can simplify the Eq. (2.1.2) into the form of Eq. (2.1.3):

$$S_D \propto f(\theta_D) + \int_0^{E_{SE\,\max}} g(\theta_D) dE_{SE} \tag{2.1.3}$$

E_{SEmax} is the maximum energy of SE. Generally, 50 eV is used [4].

S_D only accounts for the signal strength taking into account an emission point and the related detection point. In reality, the electrons are emitted into a volume of which we can only access the solid angles the detector covers [16]. Therefore, we define the experimentally accessible effective signal strength, S_E and use this parameter instead of S_D in the following calculation, as described in following Eq.:

$$S_E = S_D*\cos^2\theta_D \propto [f(\theta_D) + \int_0^{E_{SE\,\max}} g(\theta_D) dE_{SE}]*\cos^2\theta_D \tag{2.1.4}$$

2.2. Calculating the detected electron signal based on electron emission in a beam deceleration field

When a deceleration field is applied on the SEM sample, $\theta_D = \theta_S$ is no longer valid. Hence, estimating S_E, involves a transformation of the electron angular distribution from axis based on θ_S to one based on θ_D using Eq. (2.2.1). This is derived more fully in the supporting information for flat sample surfaces and flat detector surfaces which are large enough such that the deceleration field is a uniform parallel electric field E_d, between the surface and the detector plane in which the emitted electron (with charge q) is uniformly accelerated. Then E_d is determined by the working distance, and the applied deceleration voltage, U_d.

$$\theta_D = \tan^{-1}\left[(\sqrt{2E_e\cos^2\theta_s + 2U_d q} - \cos\theta_S\sqrt{2E_e})\frac{\sqrt{2E_e}\sin\theta_S}{U_d q} \right] \tag{2.2.1}$$

E_e is the electron scattering energy, which is equal to E_{SE} or E_{BSE}, dependent on its origin.

We obtain an expression with θ_D instead of θ_S for the effective BSE signal, $S_{E(BSE)}$ as derived in the supporting information and shown in Eq. (2.2.2).

$$S_{E(BSE)} \propto \int_{\theta_{D\,\min}}^{\theta_{D\,\max}} [(E_{BSE}\cos\theta_D + U_d q - E_T)\cos^2\theta_D * P_{BSE}(\theta_D)] d\theta_D \tag{2.2.2}$$

The effective SE signal, $S_{E(SE)}$ depends on the value of U_d. When $E_T > U_d\ q + 50$ eV, the SEs will reach the detector but if their energy is below the threshold, the detector will not yield any SE signal. In the case that the $E_T < U_d q + 50$ eV, SEs that reach the detector threshold will contribute to S_E but then becomes a mixed SE/BSE signal. The contribution of the SE to the mixed signal is $S_{E(SE)}$ and given by Eq. (2.2.3) as described in supporting information SI 2.

$$S_{E(SE)} \propto \int\int [P_{SE}*\cos^2\theta_D*(E_{SE}\cos\theta_D + U_d q - E_T)] dE_{SE} d\theta_D \tag{2.2.3}$$

3. Experimental methods

3.1. Monte Carlo simulation of the scattered electron distribution

The electron emission of the sample was simulated from the Monte Carlo program [18] using the following inputs(full list in Table 3.1.1): the material composition (average atomic number), electron affinity, electron energy loss function (EELF) as well as the impact angle and U_L of the primary electron. Since the Monte Carlo simulation is based on the Mott cross-section for BSE and the dielectric function approach for SE, only full energy loss function (EELF) input for single element materials were used. The EELF inputs are energy, width and strength of each oscillator.

The simulation is based on the electron banding and atomic composition of the material; the crystallinity or orientation is not a direct input parameter. However, such structural differences would affect the density input, thus would lead to a difference in the simulation result. For example, the amorphous/crystalline phases are represented by the respective density inputs in our simulation for P3HT samples in Section 4.2.2.

The primary electron energy input, E_0, is the landing energy of the primary electron. Thus the simulation result is not affected by a deceleration field for a chosen E_0, and any situation in which the primary electron cannot reach the sample before (e.g. it is deflected by the deceleration field) is not considered here. The

Table 3.1.1
Monte Carlo simulation inputs for various samples.

Sample	Amorphous C	Cu	PNIPAM	PEGDA	P3HT
Unit composition	C	Cu	$C_6H_{11}NO_2$	$C_2H_4O_2$	$C_{10}H_{14}S$
Molecule mass (g/mol)	12.011	63.546	113.158	44.050	166.288
Density (g/cm^3)	1.700	8.960	1.100	1.120[a]	1.090 (amorphous)1.132 (crystalline)[b]
Electron affinity /Work function (Ev)	4.260	10			2
EELF oscillator electron energy parameter	6.260, 25.710	17.800, 27.700, 31.500			2.740, 23.400
EELF oscillator width parameter	5.710, 13.330	3.250, 7.100, 61.700			0.325, 16.100
EELF oscillator amplitude parameter	0.236, 0.709	0.0281, 0.0925, 0.928			0.00899, 0.740

The average atomic numbers of PNIPAM and PEGDA are respectively 3.26 and 3.42.

[a] The density of PEGDA used in simulation input above is the average density of the composite matrix.

[b] The density of amorphous and crystalline phase P3HT is acquired from literature [31].

electron angular distribution was acquired as the probability for each scattering angle in the range of 0–90°, with a step size of 1°. The electron energy distribution was acquired as the probability of electron energy from 0 eV to E_0+5 eV (in order to cover the width of the elastic peak), in energy steps of 0.1 eV. The SE distribution was simulated from 0 to 100 eV scattering electron energy in order to cover the tail of SE peak, while the low-loss BSE were simulated from E_0-100 eV to E_0+5 eV in order to cover the plasmon-loss and elastic peak. In the case of the electron energy-angular distribution of SE, the data was acquired from simulating the angular distribution of 0–1 eV, 1–2 eV, …, 99–100 eV scattered electrons. Every 1 eV step and the distribution was built from the collected probability points in an electron energy-scattering angle-probability coordinate system. The data sets acquired from simulation was plotted and processed with Savitzky-Golay smoothing.

3.2. Sample materials

The Cu and amorphous C sample used, obtained from Agar, were 200 Mesh TEM copper grids with carbon film. The carbon film had a thickness of 13 nm (which is smaller than the maximum penetration depth of a 2 keV electron beam.) In order to prevent the electron signal transmission, we created another 4 μm thick C layer by an Emitech C coater, the layer thickness requirement is discussed in SI 3. The electron implantation and the "bulk" thickness requirement is simulated by Monte Carlo simulation. Detail of relationship between film thickness and electron interaction is discussed elsewhere [32].

The PNIPAM/PEGDA semi-interpenetration network was fabricated with highly branched PNIPAM and a PEGDA matrix. Synthesis of the PNIPAM system is described elsewhere [33]. The PNIPAM concentration of the sample investigated was 20% wt. To enhance conductivity and remove contamination, the PNIPAM/PEGDA samples were plasma etched in air by a Diener Zepto version B (840 s and 100 W power).

The P3HT was purchased from Ossila, brand Merck SP001 94.2% regioregularity and $M_w=54{,}200$ Da and spin coated on silicon substrate from solution. The detail of the P3HT film is described elsewhere [34].

3.3. SEM image acquisition

The SEM images were taken in a FEI Nova450 SEM. The contrast and brightness setting of the microscope was set to fixed values for each CBS detector segment in all data sets. The background subtraction of the images was done by taking reference images with beam blank for every setting in the imaging process. The detection angle of each CBS segment is calculated from the detector segment size and microscope working distance as shown in Fig. 3.3.1, while the detector segment size is measured from an image of the CBS detector. In order to change the detection angle, the microscope was operated to record images from a series of working distances with fixed U_L and U_d.

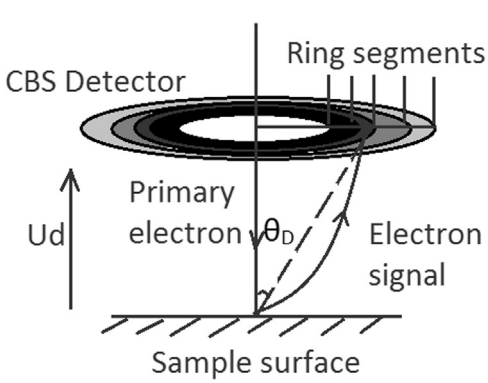

Fig. 3.3.1. A schematic of the parameters of CBS detector, the θ_D can be directly calculated from working distance and segment location.

All data sets were acquired with fixed U_L and either 1) fixed U_d while changing the detection angle θ_D or 2) changing U_d with fixed θ_D.

The measured grey value extracted from the image (8 bit) using ImageJ 1.48 v software represents the signal intensity S. Grey values for all individual pixels were averaged from the entire field of view before the reference value is subtracted. This reference value is determined by averaging all grey values present in an image with same field of view and identical microscope settings but with a blanked beam.

4. Result and discussion

4.1. The comparison of simulation and experimental data of SEM signal on a single element material

In order to test the feasibility of the simulation, we investigated two single element materials: Cu as an example of a heavy element and amorphous carbon as an example of light element. The data of these two samples is well established in literature [35–37] and was used to provide a good comparison between our simulation and experimental data.

4.1.1. Comparison of simulation and experimental non-decelerated BSE signal

Fig. 4.1.1a and c are plots of experimental BSE signal versus the simulated signal calculated from MC simulation from the 17–38° θ_D range. We note that the experimental intensity vs simulated intensity data remains linear from 18° to 32° for Cu (see Fig. 4.1.1a) and 17–34° for amorphous C (see Fig. 4.1.1c).

At larger θ_D, the experimental signal intensity drops noticeably below the predictions from MC simulations. We consider the angle up to which the prediction fits as the upper limit of the angular range for which our model is valid. We have not observed any signal intensity deviation from our predictions at the minimum accessible angle (17°) of our detector. As shown in Fig. 4.1.1b and d, the shaded area is the actual valid prediction zone in the simulated intensity angular distribution curve for our CBS detector in the absence of a deceleration field. In the absence of a deceleration field any SE contribution to the signal can be ignored as it is below the detector energy threshold E_T, which we estimate to be around 400 eV from our imaging experiments.

4.1.2. The prediction of the influence of the SE signal in a decelerated SEM imaging process

The SE signal can exceed the detector threshold of a BSE detector if the applied deceleration field results in SE energies larger than E_T+50 eV, thus the simulation of the SE signal is required for the identification of signal detected in these situations. The simulation of SE signal relies on the energy-angular distribution of SE emission. This is shown in Fig. 4.1.2(a) the SE distribution is focused in a small energy range below 30 eV for the Cu sample with U_L 2000 eV. The SE distribution covers the whole angular range of 0–90° but reaches a maximum at around 40°. $S_{E(SE)}$ only contributes to S_E if two conditions are fulfilled, that is, the threshold of the detector needs to be exceeded and the maximum θ_D is brought within the angular range of the detector through the effects of E_d. Since E_d is perpendicular to the detection plane and much larger than the SE energy, the actual $S_{E(SE)}$ is very small. For example, for Cu with $U_L=2000$ eV and $U_d=1000$ V deceleration field, an SE with 50 eV energy would have the maximum θ_D when

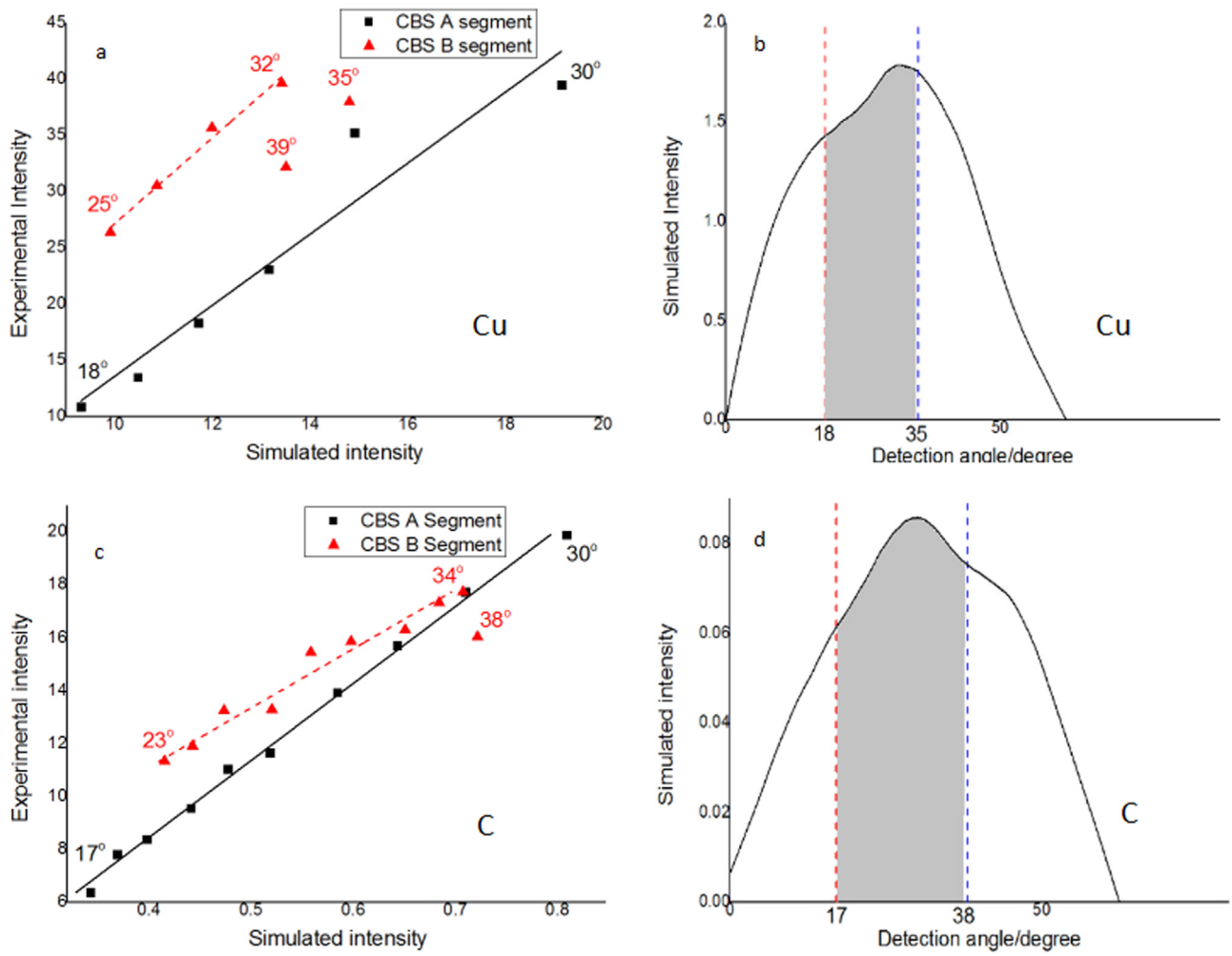

Fig. 4.1.1. (a, c): Plots of experimental (U_L=2000 eV, U_d=0) intensity versus the simulated intensity of Cu (a) and amorphous C (c); (b, d): Simulated $SE_{(BSE)}$ signal as function of θ_D for Cu (c) and amorphous C (d), the shaded areas indicate the range of experimentally accessible angles for which the simulation method remains valid.

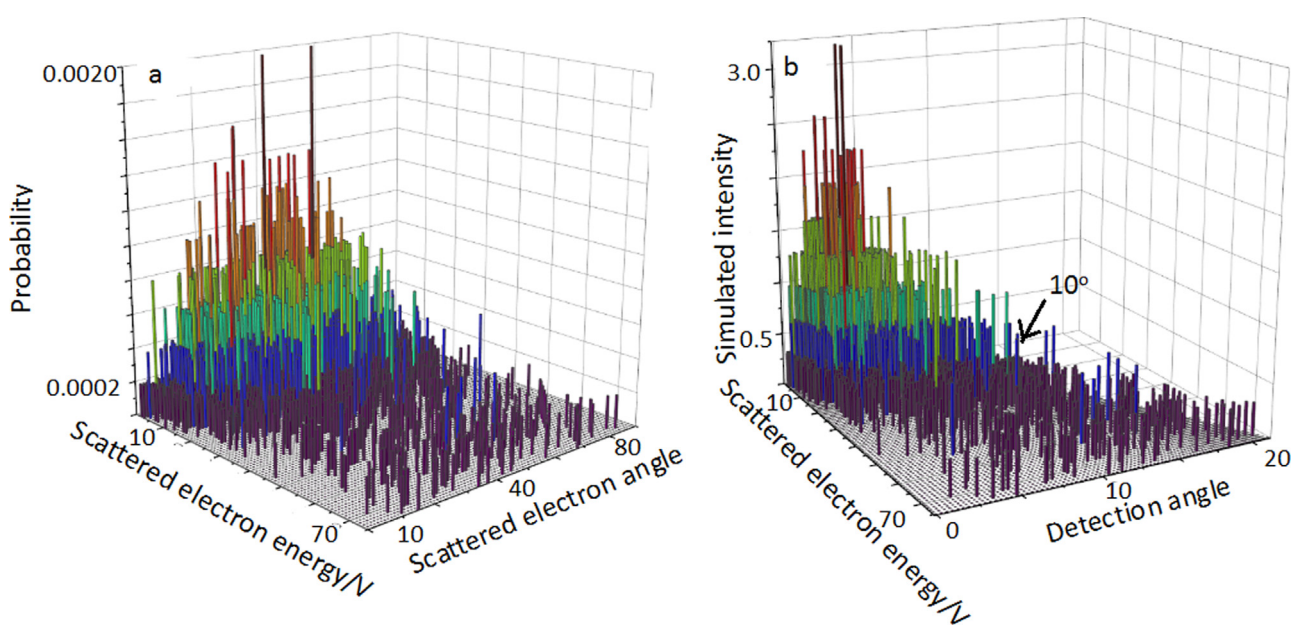

Fig. 4.1.2. (a) The electron energy-scatter angular distribution of Cu with U_L=2000 eV, U_d=0 V; (b) the simulated $S_{E(SE)}$ distribution of the same sample when U_d=1000 V. The scatter in the higher energy (50–80 eV) part of the data is a result of the very low electron probability (< 0.0002 for each scattered purple data point and < 0.5% of the total SE emission) as shown in (a).

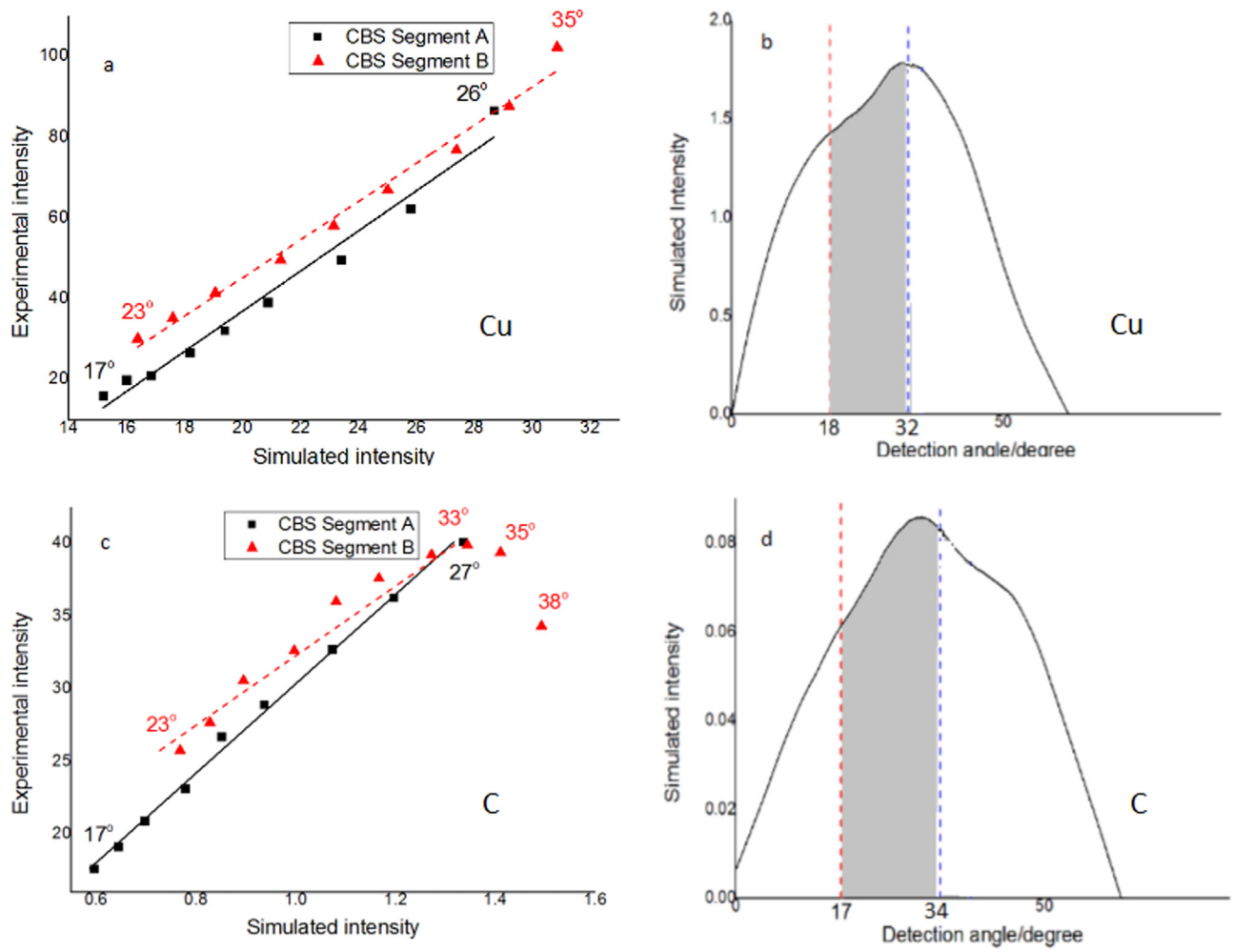

Fig. 4.1.3. Plots of experimental (U_L=2000 eV, U_d=1000 V) intensity versus simulated intensity of Cu (a) and amorphous C (c); (b, d): Simulated $SE_{(BSE)}$ signal as function of θ_D for Cu (c) and amorphous C (d), where the shaded areas indicate the range of experimentally accessible angles.

it is emitted parallel to the detection plane. That θ_D would then only be 17° which is the lower limit for the CBS detector in our microscope.

As shown in Fig. 4.1.2(b), the SE will only form a large signal in very small detection angular range below 10° for the Cu sample. Although other materials have different SE distribution, the SE detection range is still always limited below 15° for all our samples and microscope settings. The SE signal intensity peak also shifts to smaller θ_D if the U_d is increased, and so the SE signal can safely be ignored.

4.1.3. Comparison of simulation and experimental decelerated BSE signal

As shown above, the SE signal can be safely ignored for the CBS detector in our SEM conditions, even if a deceleration field is applied. Hence the main difference of the results presented in Section 4.1.1 (where U_d=0) is a substantial increase in $S_{E(BSE)}$ that falls within an angular range of our CBS detector (compare Fig. 4.1.1a and c (U_d=0 V) and Fig. 4.1.3a and c (U_d=1000 V)). However, according to the experimental versus simulated data plot shown in 4.1.3a, c, the valid θ_D range for simulation to match experiment is still limited to around 35° for both the Cu and the amorphous C samples. Furthermore, slight changes in the angular distributions are visible when comparing Fig. 4.1.1b,d (U_d=0 V) and Fig. 4.1.3b,d (U_d=1000 V). Note especially the more pronounced peaks and shoulders appearing in Fig. 4.1.3b, d. The detection angle zone that is validated by our experiment (shaded in grey in Fig. 4.1.3b, d) still extends just past the maximum for Cu in Fig. 4.1.3b and the first peak in Fig. 4.1.3.d obtained for amorphous C. For larger angles, the experimental intensity still drops rapidly below the predicted value for angles larger than 35° for Cu and 38° for C sample (Fig. 4.1.3b, d).

4.1.4. The estimation and effect of angular distribution of the BSE_I and BSE_{II} signal

As mentioned in the introduction, the BSE emitted from the very top surface of a specimen forms a signal which is topography dependent. This BSE_I signal is emitted at a large scattering angle. If we plan to acquire a BSE image with solely compositional contrast, we need to collect the BSE_{II} signal which is emitted from beneath the sample surface. The BSE emission simulated from different layers within the specimen from 0 to 0.5 nm to full penetration depth of Cu and C. As shown in Fig. 4.1.4a, c, the scattering angle of the highest electron probability/intensity shifts from 83° to 75° for C and 76–51° for Cu. The same trend is also observed in Fig. 4.1.4b, d for the simulated relative BSE intensity when a U_d=2000 V is applied.

Although there is no clear boundary for the BSE_I and BSE_{II}, the electrons emitted from the first 3 nm of the sample surface have an emission depth which is very similar to SE and can be expected to contribute to the topographical contrast of BSE images. As can be seen from Fig. 4.1.4. the BSE_I signal constitutes a large fraction of $S_{E(BSE)}$ for both C and Cu. Hence in these cases, topography can significantly affect BSE imaging. This effect can be noticed as

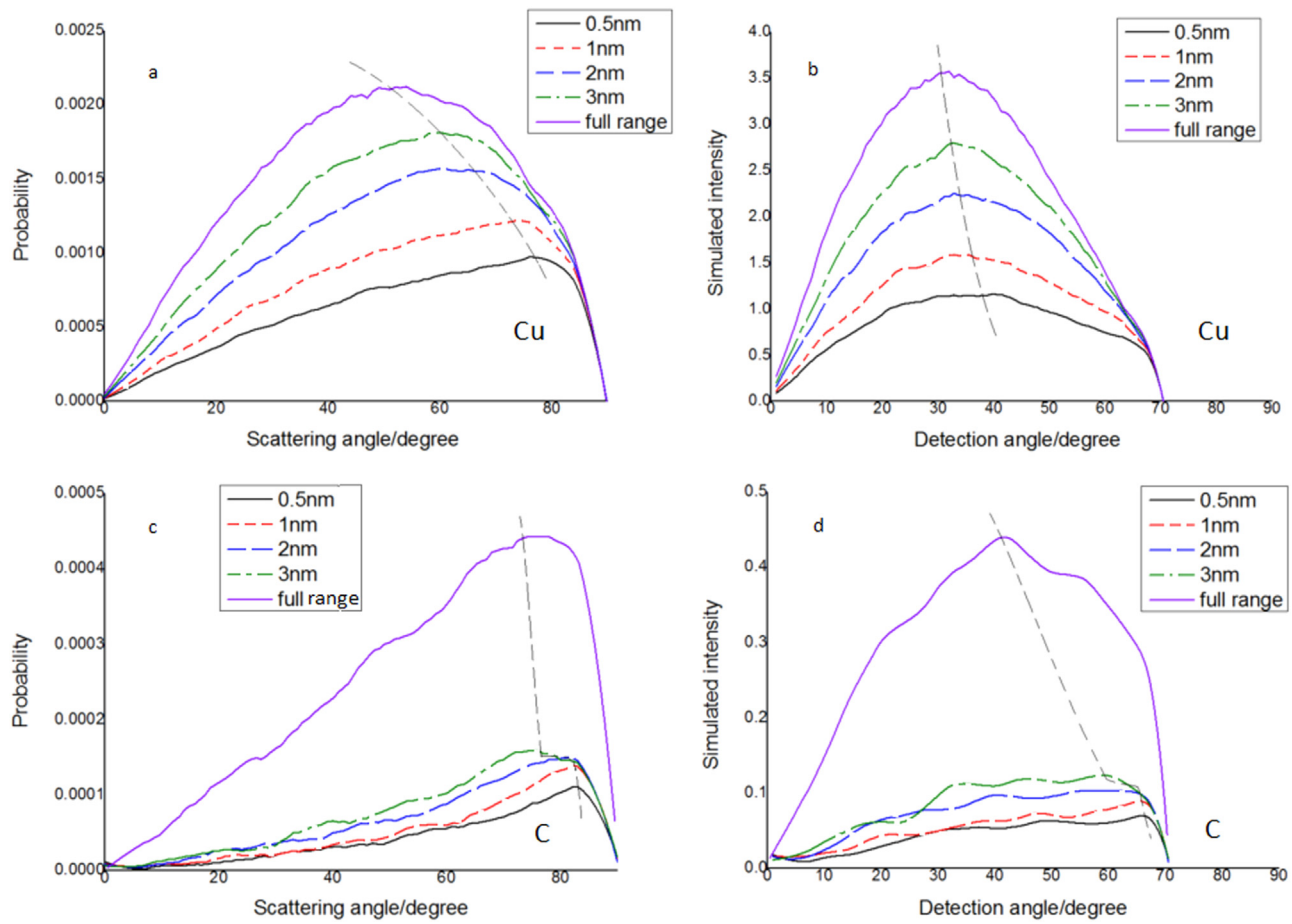

Fig. 4.1.4. (a, c) The simulated BSE angular emission with varying thicknesses of emission layer for Cu (a) and C (c) at U_L=2000 V; (b, d) Simulated intensity based on emission shown in (a, c) when U_d=1000 V. The peak of each angular distribution curve has been connected by a dashed line. The full range curve represent the full implantation range BSE, which is a reflection of BSE_{II} in this case.

shoulders or even double peaks in the BSE angular distribution curve such as in Fig. 4.1.3b, d. The fact that BSE_I is the dominant signal for BSE detection at large angles (see Fig. 4.1.3b, d) also explains the substantial deviation of simulated intensity from experimental data for larger θ_D as we do not control the surface topography. Hence nano-scale topography limits the validity of our prediction range of angles just below the first peak in the angular emission plots. For this range, the BSE image contains purely compositional information. The more this angular range is exceeded toward larger angles, the stronger the contribution of topography to the detected BSE signal. This effect can indeed be exploited for the measurement of nano-scale topographical features as reported in [12]. Importantly, this shows that by correctly choosing the maximum θ_D, topographical and compositional contrast can be selected. As the SEM user does not select this angle directly but needs to achieve it through the correct combination of working distance, U_L, U_d and detector segment, this model can be used to predict the best combinations for maximum compositional contrast.

4.2. Application of model for the optimisation of compositional BSE signal on complex nanostructured materials- PNIPAM/PEGDA semi-IPN and regioregular P3HT film

Section 4.1 shows that in the cases of single elemental samples of Cu and amorphous C, the prediction of the BSE signal intensity is reliable in the angular range from largest SE detection angle to the first maximum in the simulated angular distribution. As shown by the results of the Cu sample this simulation can be applied to heavier elements, but our main purpose is the optimisation of polymer imaging as these are the most challenging of materials due to often minute differences in average atomic numbers.

Here we extend the same prediction, thus the microscope setting (detection angle limitation) for a guaranteed optimisation of composition contrast can be achieved to exclude contributions from topography.

4.2.1. Verification of simulated BSE signal and experimental signal of a PNIPAM/PEGDA semi-IPN

The same verification method used in 4.1 to check the feasibility of our prediction has been applied on the PNIPAM/PEGDA semi-IPN samples and the plot of the simulated intensity versus experimental grey value is shown in Fig. 4.2.1. The highest usable primary beam voltage for this polymer composite is limited to around 1 kV due to charging effects. The experimental signal for this condition without deceleration field is very small and the imaging at U_d=0 V is not practical. Hence the only data checked for the PNIPAM/PEGDA sample are those with deceleration applied using the methods of Section 4.1.3.

The PNIPAM simulation in Fig. 4.2.1 compares and fits the experimental data to the maximum angle of around 29°. The angle that this linear relationship ends is around the same value for both the A and B segment in our CBS detector. The PEGDA simulation only fitted with experimental data to the maximum angle of around 26°, which resulted in the simulation deviating from linear relationship in almost the entire angular range of the B segment (23–40°).

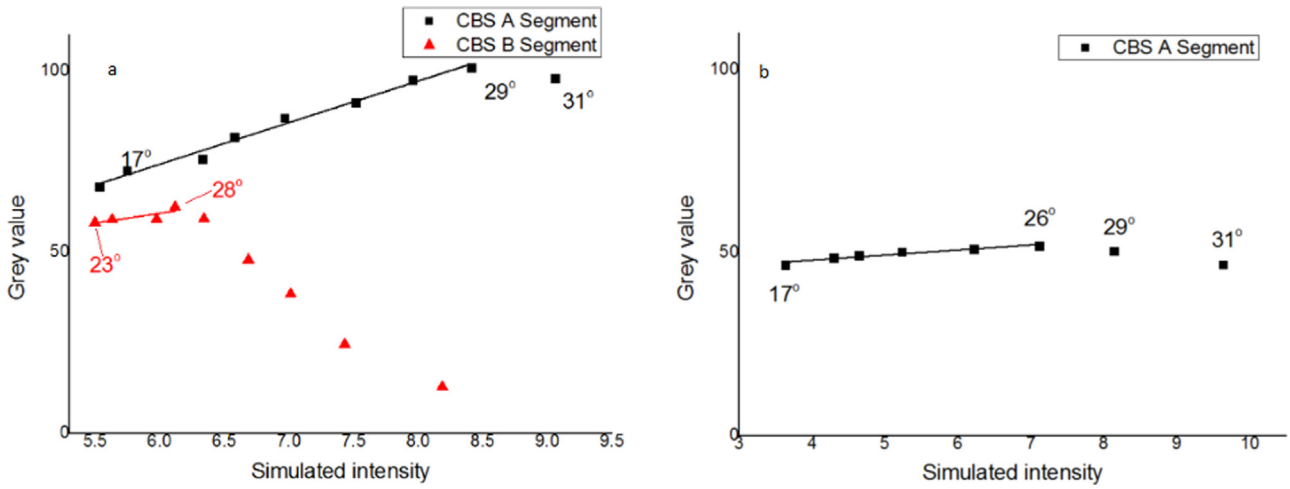

Fig. 4.2.1. The plot of simulated BSE signal intensity with the experimental image grey values using U_L=1000 V and U_d =4000 for (a) PNIPAM and (b) average value of PEGDA matrix.

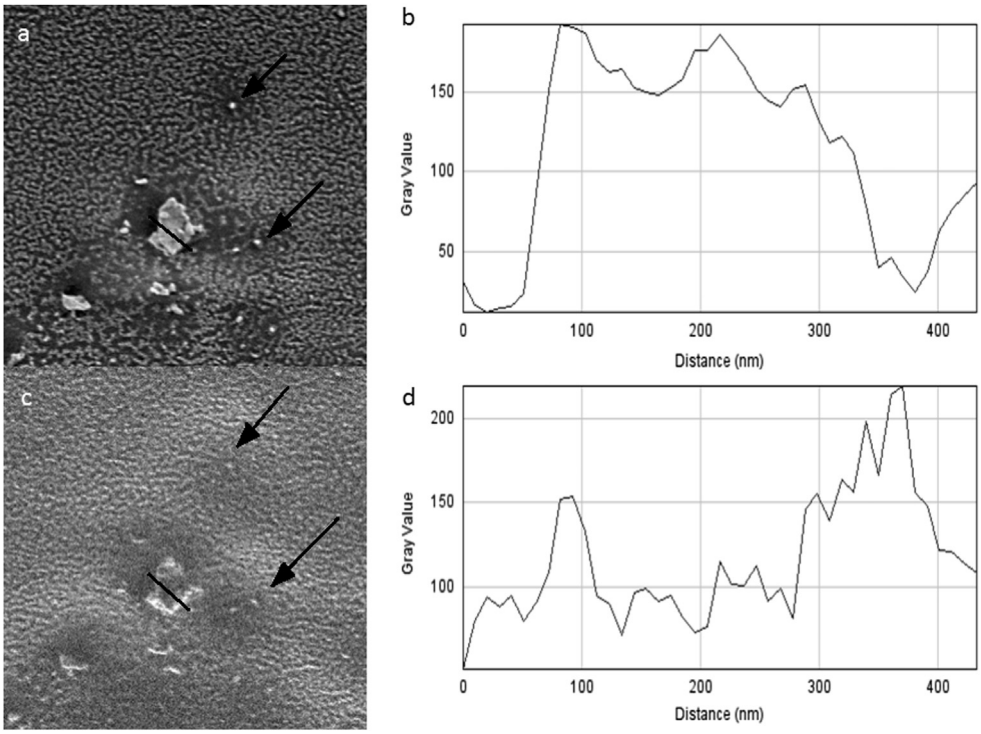

Fig. 4.2.2. The CBS image of the surface of PNIPAM/PEGDA sample from (a) segment A (14–22°) and (c) segment D (30–36°) both with U_L=1000 V and U_d=4000 V. The field of view is 3*3 μm^2. The location of small PNIPAM particles are highlighted by arrows; (c, d) are the corresponding line profiles of the larger PNIPAM particle in (a) and (c).

Fig. 4.2.2a is an image taken within our predictable angular range that results in compositional contrast. This polymer composite contains PNIPAM particles with size from 50 to 200 nm as well as smaller 30–50 nm features in PEGDA matrix. PNIPAM particles (indicated by the arrows) yielded larger signal than any part of the PEGDA, as expected from results in Fig. 4.2.1. The same locations are indicated in Fig. 4.2.2b, which was taken at angles exceeding our predictable range, and thus contain little compositional contrast. The contrast is mainly formed by the topography difference between different phases created in etching and indeed the small PNIPAM particles are barely visible. The larger PNIPAM particle at the centre of the image can mainly be recognised by its bright edges. The line profiles of the two images in 4.2.2 b, d also confirm this. The appearance of edge effect (the high brightness edge formed at steps on sample surface due to the small emission depth of the relevant electron signal [38]) is a clear sign of the appearance of topographical contrast. Since the large angle signal is dominated by BSE_I, the topographical BSE images for large angle agree with our expectation based on simulation in 4.1.4. Thus we can use the BSE below the simulated peak in the angular distribution for composition contrast imaging and select the BSE at large angles for topographical imaging.

4.2.2. Limitation of the signal prediction

Comparing the data acquired from the PNIPAM/PEGDA sample (Fig. 4.2.1) and the single elemental samples of Cu and C (Fig. 4.1.3), the viable angular range of our prediction method changed dramatically for each different material and different imaging conditions. However, this viable angular range is closely related to the simulated angular distribution peak in our

Table 4.2.1
Comparison between the peak position in simulated angular distribution and the maximum reliable prediction angle obtained from experiment.

Specimen	Simulation Intensity peak position/degree	Experimental Maximum reliable angle for our prediction/degree
Cu	32	32
C	31	34
Cu (U_d=1000 V)	34	35
C (U_d=1000 V)	33	33
PNIPAM (U_d=1000 V)	28	29
PEGDA (U_d=1000 V)	24	26

simulations. The maximum angular range are shown in Table 4.2.1, this maximum viable angle value always matches the peak position of the simulated intensity distribution curve (shown in Fig. 4.1.4) as the maximum in the BSE_{II} peak and highlighted by the dashed line.

As stated earlier in 4.1.2, since the energy of the major part of the SE is always around 0–50 eV, we always expect the SE to be limited to very small angular range ($<10^{o}$) for any U_d above 1000 V. Hence we can conclude that the viable angular range for our BSE signal prediction is from 10° to around the angle of the simulated angular distribution peak.

Ideally for a known material, the detection angle limitation can be chosen at the angle of the simulated angular distribution peak that is obtained from the simulation. We demonstrate this on the example semicrystalline polymer presented in Section 4.2.4.

4.2.3. Microscope settings for optimised signal simulation of PNIPAM/PEGDA semi-IPN

According to 4.2.2, we can estimate the expected angular range for our BSE signal for known microscope settings and materials. Since the angular range in our CBS detector is fixed, the working distance is changed in order to select the θ_D range as shown in Fig. 4.2.3. To utilise this figure for the optimisation of compositional contrast we must use the range in which topography will not affect the contrast. This range is based on the results of Fig. 4.2.1 and indicated by striped lines in Fig. 4.2.3. It can be seen that the detector segment A can deliver compositional contrast over a much wider range of working distances than segment B. However, the simulations in Fig. 4.2.3a and c show that the compositional signal intensity obtainable with detector segment B is substantially higher than that from segment A, due to a slower reduction trend of the overall intensity in segment B as θ_D decreases. This leads to higher noise-signal ratio in high contrast setting in segment A and makes segment B a more suitable segment for high contrast imaging at large working distances, as shown in experimental data in Fig. 4.2.4a. This situation demonstrates the complexity of optimising the contrast on an experimental basis. A further parameter that the user has to decide is U_d, which can also have a substantial influence (see Fig. 4.2.4b).

Moving from overall simulated signal intensities to simulated contrast, where contrast is defined as $C=\frac{S_2-S_1}{S_2}$ (S_1, S_2 is the grey

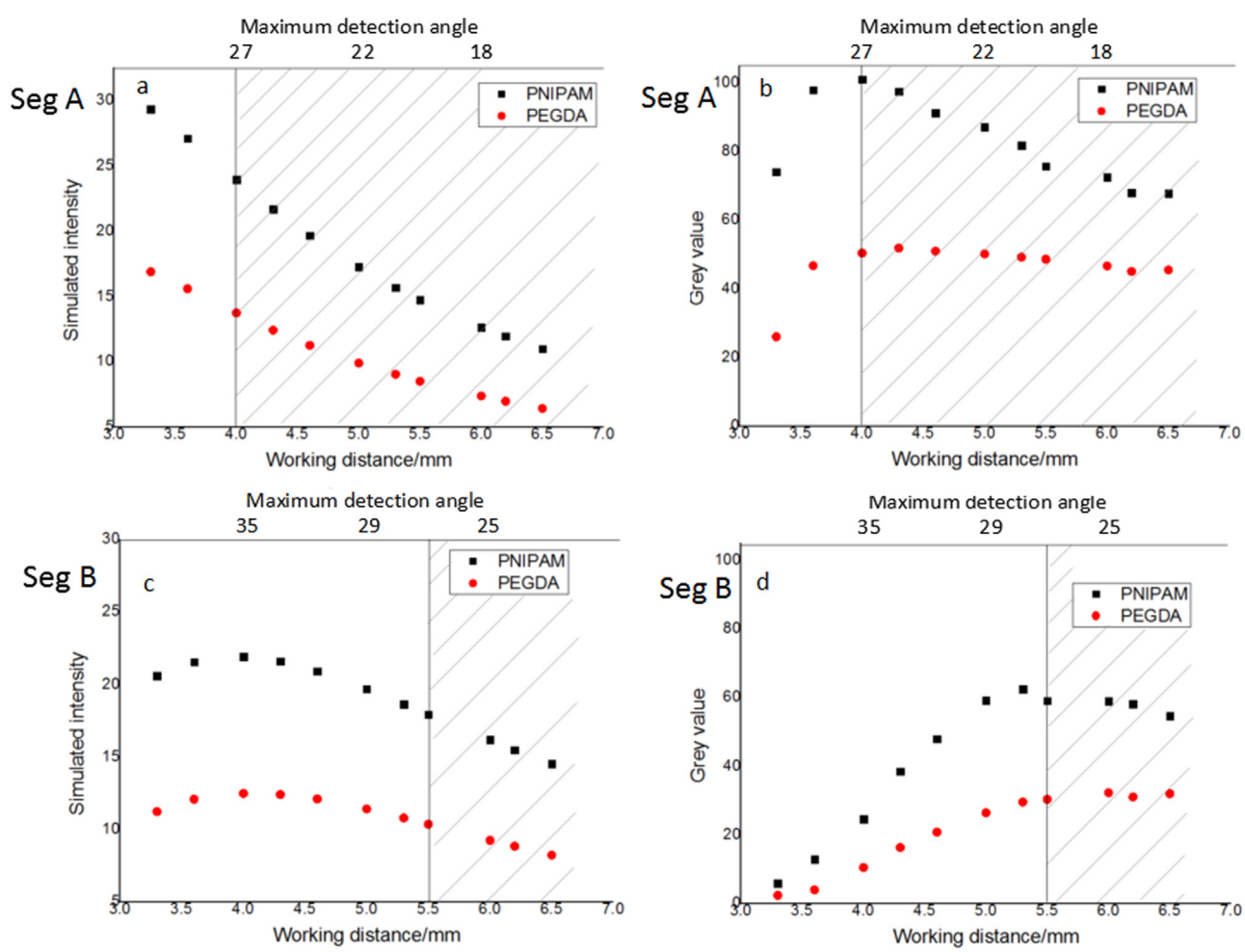

Fig. 4.2.3. (a) Simulated intensity for PNIPAM and PEGDA with U_L=1000 V and U_d=4000 V using segment A of CBS; (b) Experimental image grey values for same conditions as in (a); (c) as (a) but using segment B of CBS; (d) as (b) but using segment B of CBS. The predictable zone for our model is marked by the striped area.

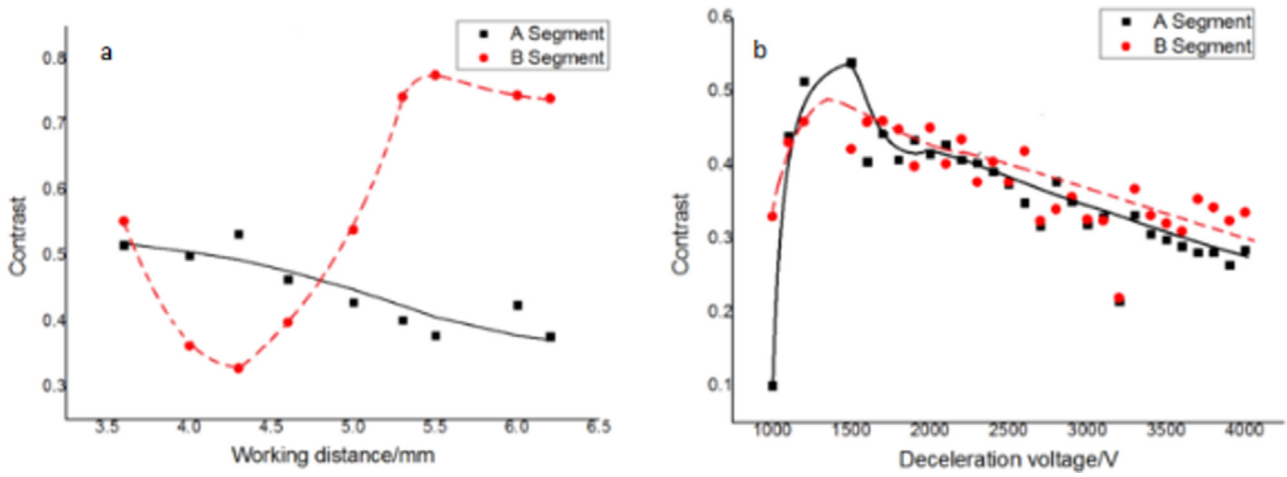

Fig. 4.2.4. BSE images collected with CBS segment A and B at $U_L = 1000$ V (a) Experimental contrast between PNIPAM and PEGDA versus working distance; (b).

value of different areas, $S_2 > S_1$) [17]. The simulated contrast can be plotted as a function of both U_d and θ_D (see Fig. 4.2.5a). This plot immediately indicates on how to maximise the contrast. However, we need to bear in mind that only a limited angular range delivers pure compositional contrast. Therefore, in Fig. 4.2.5b the line of maximum reliable contrast is projected into the U_d versus θ_D plane and plotted. Any microscope settings that lead to detection within the striped area in Fig. 4.2.5. will give pure compositional contrast. Maximum compositional contrast is obtained with settings approaching the line of maximum contrast from the smaller θ_D. Thus we can select any experimentally realisable θ_D–U_d pair near this curve for optimised compositional imaging. This θ_D can be directly transferred to the location of concentric ring detector segment based on the location of working distance setting as mentioned in calculation 2.2. Since the concentric ring detector has an angular range, in order to acquire reliable compositional contrast, maintaining the maximum θ_D of the chosen segment in Fig. 4.2.5 a is suggested. The position of this curve for a given set of materials is determined by the highest angle for valid compositional contrast prediction of this material system. This can be experimentally verified as shown in Fig. 4.2.1.

For some settings within the predictable zone in Fig. 4.2.5b, the contrast could reach higher values than our suggested setting as the total signal intensity drops at low U_d and low θ_D. However, as shown in Fig. 4.2.6c, this higher contrast is accompanied with a low signal intensity and hence low signal to noise ratio. Our suggested setting at the maximum valid angle provides a high intensity difference and a high total signal intensity as shown in Fig. 4.2.6a.

Our simulated optimised contrast settings in Fig. 4.2.5(b) were compared with the experimental optimised contrast setting for PNIPAM/PEGDA specimen. The experimental optimised contrast setting was acquired from contrast-U_d plot at working distance 4.5–60 mm similar to the plot in Fig. 4.2.4(b). As shown in Table 4.2.2, the experimental and estimated optimised setting agrees well. The absolute deviation from our estimated setting is about 200–300 V for most conditions. Therefore, higher U_d results have shown smaller relative differences to our simulations. We recommend that this simulation method be used for the optimisation of the compositional contrast collected from specimens with small compositional changes. It can be directly translated into suitable experimental settings using plots such as shown in Fig. 4.2.5a, b. In this way, polymer nanoparticles in multi-phase polymer systems can successfully be predicted, imaged and identified.

4.2.4. Application of model to imaging crystallinity in regioregular P3HT film

Another example application of this method is P3HT which is a conjugated, semiconducting polymer commonly used as a film in

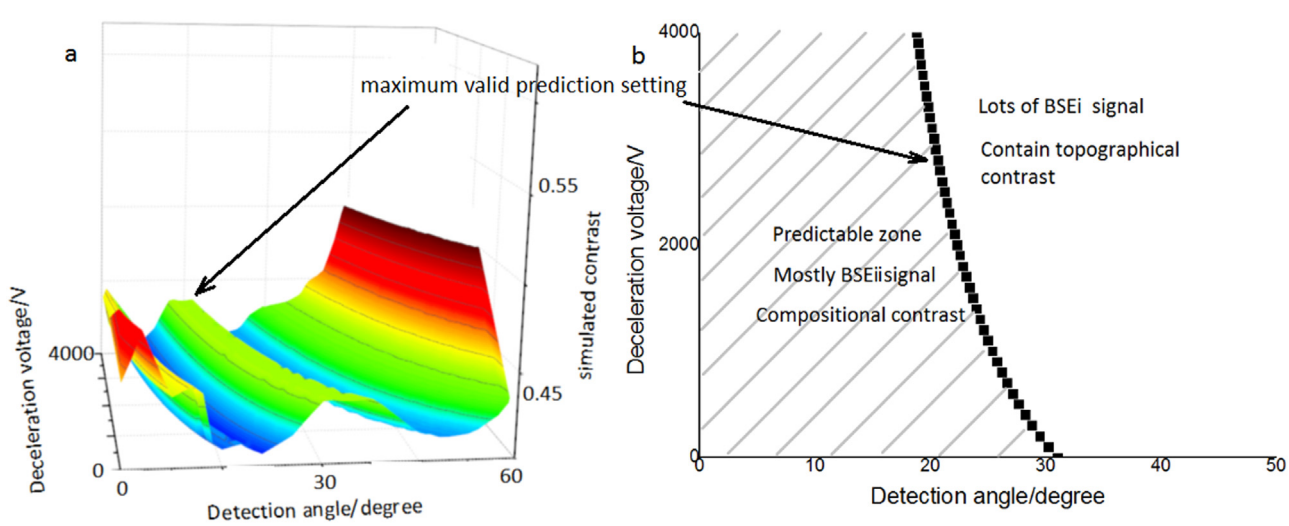

Fig. 4.2.5. The BSE simulated contrast vs U_d and θ_D of PNIPAM/average PEGDA matrix (a) in 1000 V U_L condition. The contrast peak position was projected as a curve in 2D θ_D-U_d plane (b). The predictable zone is marked with striped area in b. Note the U_d is limitation by the accessible range of the microscope.

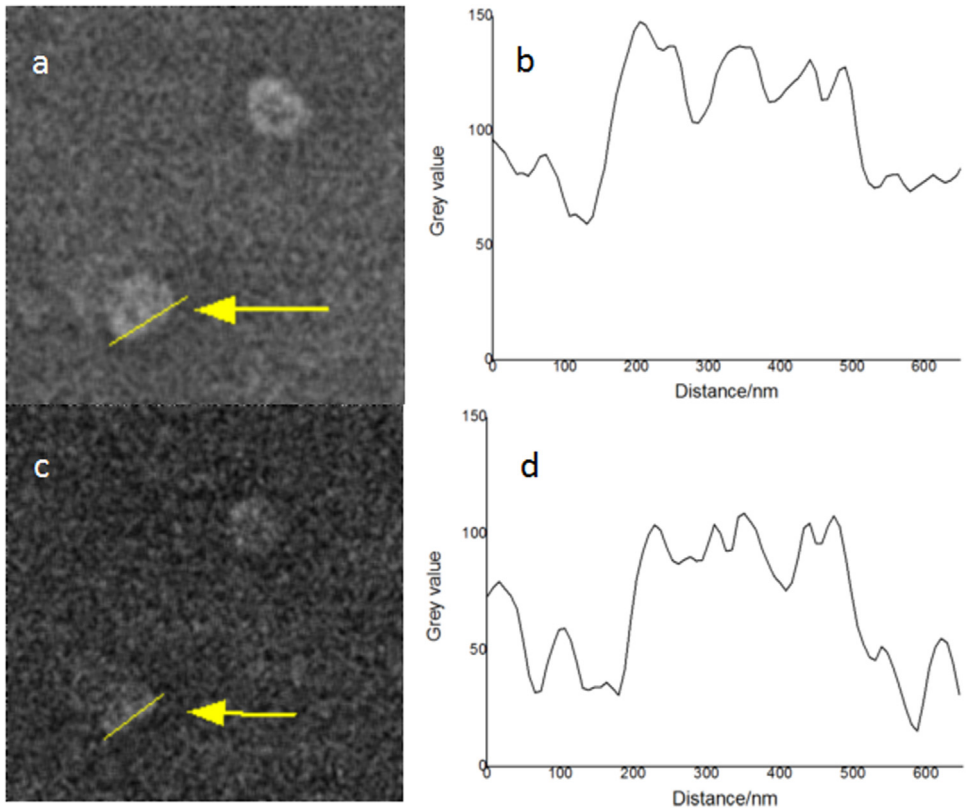

Fig. 4.2.6. The images a and c are CBS B segment images taken at $U_L = 1000$ V working distance 4.5 mm for PNIPAM/PEGDA sample. The Ud is 3000 V for image a and 1700 V for image c. The Fig. b and d show the corresponding line profiles of the PNIPAM particle on image a and c, the line is indicated by arrow on image a and c. The field of view is 2*2 μm^2.

Table 4.2.2
The comparison between estimated and optimised experimental settings for PNIPAM/PEGDA sample from working distance 4.5–6 mm.

Working distance (mm)	**Simulation** Optimised deceleration voltage (V)		**Experimental** Optimised deceleration voltage (V)	
	Segment A	Segment B	Segment A	Segment B
6	–[a]	3214	–[b]	3500
5.5	4729	2235	–[b]	2500
5	3890	1461	4000	1800
4.5	3119	841	2900	1100

[a] This voltage is over 10 kV and exceeds our assumption of the electron speed in primary beam axis $v_{ey} < 15\%$ c (c is speed of light) as mentioned in supporting information 1.

[b] These values exceed the upper limits of the deceleration voltage obtainable in our microscope.

organic electronic devices. It has a semicrystalline structure and the level of crystallinity in a P3HT film is strongly linked to its performance in electronic devices [39]. Generally, higher crystallinity in a P3HT film gives an improved charge mobility and stability. Therefore, many techniques are employed to determine the amount of crystalline phase in P3HT, but often with very different results even when measured on the same sample [40]. The often large differences are explained due to the differences in length scales that such techniques use on one hand and a more complicated scenario than a two phase model [40]. Thus here we apply our simulation to establish if crystallinity mapping via BSE imaging of a P3HT is feasible in the SEM as the latter would offer the possibility to explore crystallinity distributions on various length scales.

The microscope setting is selected by the same method described above in 4.2.3 and chosen as CBS segment A, $U_L = 1000$ V, $U_d = 4000$ V at working distance 4 mm, the settings for the crystalline and amorphous phase are simulated based on the density differences. As shown in Fig. 4.2.7a, we have collected the highest possible BSE signal for our detector segments below the angular distribution peak of BSEII. Thus a crystallinity map can be formed according to the contrast between the crystalline and the amorphous phases of P3HT. As the crystalline P3HT has reportedly a higher density the (see Table 3.1.1) our simulations predict that the crystalline phase appears brighter in the image in Fig. 4.2.7b. By analysing cystallinity mapping image collected on P3HT, associated histogram of the image can be fit into two gaussian peaks as shown in Fig. 4.2.7c. Thus we obtain the following: minor component (crystalline, ~23%) and major component (amorphous ~77%) from the respective peak areas. This composition is within the range of reported phase compositions and very close to that obtained from density measurements presented in [40]. However, our method allows us to investigate the lateral distribution best seen by thresholding the image as in Fig. 4.2.7d. to some extent. There is some overlap between the two components for grey levels below 150, we have set our threshold at 155 so to avoid such overlap. Hence, the black areas in Fig. 4.2.7 only represent the proportion of crystalline material that can be identified as such with confidence. In this context it is interesting to note that [40] suggest that a two phase model for crystallinity in P3HT might be to simplistic and intermediate degree of ordering might be present, which seem to be consistent with our observation so far. However, a much more detailed study on P3HT with different proportions of crystallinity due to different molecular weights and processing conditions, investigated at a wide range of length scales (magnifications) would be needed to test the model put forward in [40]. This is beyond the scope of this

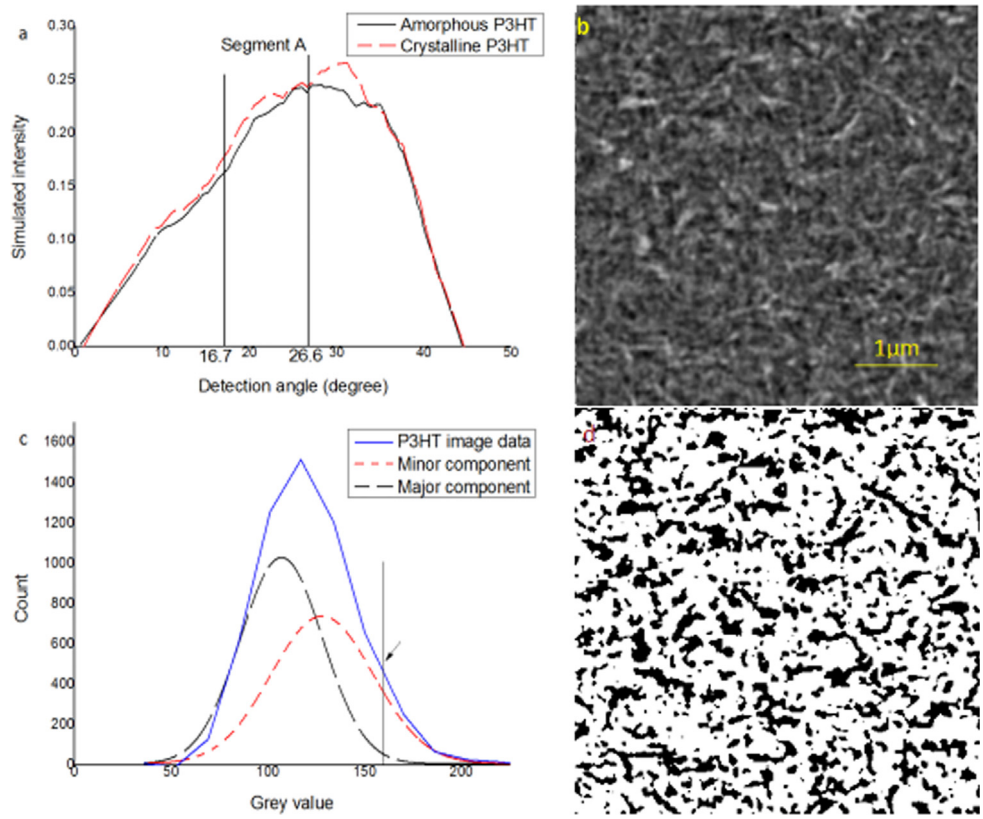

Fig. 4.2.7. The optimised microscope setting chosen for P3HT is the CBS segment A, as shown in a, this is between the minimum detector angle and the maximum valid angle (the angular distribution peak in this curve). The crystallinity distribution imaged with our setting is shown in b, the field of view of SEM image is 5*5 μm^2. The histogram of the image was fit to two gaussian peak for major and minor component in c, and by choosing threshold at the pointed grey value the crystallinity map can be acquired as shown in d.

work. The focus here is to show that our method (using simulation to ensure nano-scale chemical imaging for phases with small chemical changes) provide a new tool to investigate the subject of local crystallinity, which is of extreme importance to the field of organic electronics. The simulation data of Cu, amorphous C, PNIPAM, PEGDA and P3HT needed to apply this model can be accessed in [41].

5. Conclusion

Monte Carlo simulations of amorphous C, Cu, PNIPAM/PEGDA semi-IPN and P3HT film angular distributions of emitted electrons in a low voltage SEM have been shown. We report how to transform the simulated angular distributions to account for particular microscope settings (such as detection geometry and deceleration field,) enabling a direct comparison to experimental data and establish the angular range for which the model can be used. We found that the BSE emission for angles below the peak in the angular emission spectrum can be accurately predicted and used for contrast optimisation of compositional imaging. The BSE emission at angles larger than the peak in the angular spectrum do not match the simulations and are shown to contain mainly topographical information. Although the signal related to this part of the angular emission spectrum is not predictable by our model, the model can predict the experimental parameter range in which topographical features will influence the contrast in BSE images.

In summary our model allows us to optimise and separate compositional and topographical contrast in angle selective BSE imaging in the presence of a deceleration field. This approach can be used to solve the challenge of imaging small differences in nano-scale chemical compositions in carbon based composites or local crystallinity in semi-crystalline polymers.

Acknowledgments

Quan Wan would like to thank the Sorby Center for Microscopy and Microanalysis for the access to the electron microscope and related equipments.

Cornelia Rodenburg would like to thank ENGINEERING AND PHYSICAL SCIENCE RESEARCH COUNCIL (EPSRC, UK) for support under EP/N008065/1.

Maurizio Dapor received support from the Leverhulme Trust through the Visiting Professorship (VP1-2014-011). Maurizio Dapor also wishes to express his gratitude to Rafael Garcia-Molina, Universidad de Murcia, for his invaluable suggestions.

Appendix A. Supplementary material

Supplementary data associated with this article can be found in the online version at http://dx.doi.org/10.1016/j.ultramic.2016.09.006.

References

[1] D.L. Vezie, E.L. Thomas, W.W. Adams, Polymer 36 (1995) 1761.
[2] J.B. Pawley, Microelectron. Microsc. 83 (1992) 203.
[3] E.D. Boyes, Microsc. Micro. 6 (2000) 307.
[4] H. Seiler, J. Appl. Phys. 54 (1983) R1.
[5] R. Wuhrer, K. Moran, IOP Conf. Ser. Mater. Sci. Eng. 109 (2016) 012019.

[6] C. Gaillard, P.A. Stadelmann, C.J.G. Plummer, G. Fuchs, Scanning 26 (2004) 122.
[7] H. Jaksch, J.P. Martin, Anal. Chem. 353 (1995) 378.
[8] J.H. Butler, D.C. Joy, G.F. Bradley, S.J. Krause, Polymer 36 (1995) 1781.
[9] E.D. Boyes, Adv. Mater. 10 (1998) 1277.
[10] P. Lewis, S. Micklethwaite, J. Harrington, M. Dixon, R. Brydson, N. Hondow, J. Phys: Conf. Ser. 644 (2015) 012019.
[11] R. Bongeler, U. Golla, M. Kassens, L. Reimer, B. Schindler, R. Senkel, M. Spranck, Scanning 15 (1993) 1.
[12] E. Kieft, E. Bosch, J. Phys. D: Appl. Phys. 41 (2008) 10.
[13] Z. Czyzewski, M.D. O'Neill, A. Romig, D.C. Joy, J. Appl. Phys. 68 (1990) 3066.
[14] K. Murata, H. Kawata, K. Nagami, Y. Hirai, Y. Mano, J. Vac. Sci. Technol. B 5 (1987) 124.
[15] A.S. Pasciak, J.R. Ford, Scanning 28 (2006) 333.
[16] P. Merli, A. Migliori, V. Morandi, R. Rosa, Ultramicroscopy 88 (2001) 139.
[17] Q. Wan, R.A. Plenderleith, M. Dapor, S. Rimmer, F. Claeyssens, C. Rodenburg, J. Phys: Conf. Ser. 644 (2015) 012018.
[18] Mitsuo Suga, et al., Prog. Solid State Chem. 42 (2014) 1.
[19] R.G. Richard, G. Rh Owen, I. Ap Gwynn, Scanning Microsc. 13 (1999) 55.
[20] D.C. Joy, J. Microsc. 161 (1991) 343.
[21] J. Cazaux, N. Kuwano, K. Sato, Ultramicroscopy 135 (2013) 43.
[22] A. Sakic, et al., Micro Technol. Micro Devices Safe (2011) 1–4.
[23] I. Mullerova, I. Konvalina, L. Frank, Mater. Trans. 48 (2007) 940.
[24] T. Aoyama, M. Nagoshi, H. Nagano, K. Sato, S. Tachibana, ISIJ Int. 51 (2011) 1487.
[25] N. Erdman, V. Robertson, M. Shibata, Microsc. Microanal. 20 (**S3**) (2014) 20.
[26] C. Rodenburg, W.M. Rainforth, Acta Mater. 55 (2007) 2443.
[27] C. Rodenburg, P. Viswanathan, M.A.E. Jepson, X. Liu, G. Battaglia, Ultramicroscopy 139 (2014) 13.
[28] L. Reimer, Image Formation in Low-voltage Scanning Electron Microscopy, Tutorial Texts in Optical Engineering, Vol. TT 12, SPIE Optical Engineering Press, Bellingham, 1993.
[29] O.C. Wells, A. Broers, C. Bremer, Appl Phys. Lett. 23 (1973) 353.
[30] M. Dapor, Transport of Energetic Electrons in Solids, Springer, Tr. Mod. Phys Springer Berlin, vol. 257, 2014.
[31] X.B. Shen, W.G. Hu, T.P. Russell, Macromolecules 49 (2016) 4501.
[32] M. Dapor, N. Bazzanella, L. Toniutti, A. Miotello, M. Crivellari, S. Gialanella, Surf. Interface Anal. 45 (2013) 677.
[33] A.R. Plenderleith, C.J. Pateman, C. Rodenburg, J.W. Haycock, F. Claeyssens, C. Sammon, Rimmer Stephen, Soft Matter 11 (2015) 7567.
[34] R.C. Masters, et al., Nat. Commun. 6 (2015) 6928.
[35] B. Lesiak, A. Jablonski, Z. Prussak, P. Mrozek, Surf. Sci. 223 (1989) 213.
[36] M.R. Williams, E.T. Arakawa, J. Appl. Phys. 43 (1972) 3460.
[37] M. Dapor, L. Galliari, G. Garberoglio, Nucl. Instrum. Methods Phys. Res. B 352 (2015) 181.
[38] M.T. Postek, A.E. Vladar, Scanning 35 (2013) 355.
[39] C. Poelking, K. Daoculas, A. Troisi, D. Andrienko, P3HT Revisited – From Molecular Scale to Solar Cell Device Chapter 5 Morphology and Charge Transport in P3HT: A Theorist's Perspective, Adv. Polym. Sci, Springer Heidelberg, vol. 265, 2014.
[40] X. Shen, W. Hu, T.P. Russell, Macromolecules 49 (2016) 4501.
[41] Q. Wan, et al., Figshare, 2016, doi: 10.1513/shef.data.3838035, from ⟨https://figshare.com/s/6a00a76050231066bc1d⟩.